Journal of Materials Chemistry C

ROYAL SOCIETY OF CHEMISTRY

PAPER

View Article Online
View Journal | View Issue

Cite this: J. Mater. Chem. C, 2025, 13, 8776

High-sensitivity optical thermometer based on the luminescence of divalent and trivalent thulium ions in $CaAl_4O_7$:$Tm^{2+/3+}$ operating in cryogenic and high temperature ranges†

Rajashree Panda,‡[a] Mitrabhanu Behera,‡[a] Mahesha Hegde,[a] R. Arun Kumar, *[ab] Gunasekaran Venugopal,[c] Przemysław Woźny,[d] Kevin Soler-Carracedo[d] and Marcin Runowski[d]

Received 18th December 2024,
Accepted 13th March 2025

DOI: 10.1039/d4tc05342g

rsc.li/materials-c

Blue-emitting calcium dialuminate ($CaAl_4O_7$) phosphor doped with thulium ions was prepared *via* a microwave-assisted combustion synthesis route for the first time, and a phosphor-in-glass (P-i-G) structure was fabricated. The samples crystallized in the monoclinic structure were validated through the powder X-ray diffraction studies. A wide bandgap of 4.60 eV was observed in the $CaAl_4O_7$:Tm^{3+} phosphor. Upon excitation at 359 nm, the $Ca_{(1-x)}Al_4O_7$:$0.03Tm^{3+}$ sample generated a bright blue emission around 459 nm that was ascribed to the $^1D_2 \rightarrow {}^3F_4$ transition of Tm^{3+}. The temperature-dependent measurements (−180 to 300 °C) revealed the presence of Tm^{2+} ions as a broad-band emission centered around 500 nm at cryogenic temperatures. The unusual enhancement in the signal intensity of Tm^{3+} with varying temperature could be beneficial for general lighting technology and LED devices. Owing to the diverse thermal quenching rates and thermalization processes of Tm^{2+} and Tm^{3+} emissions, we were able to develop a highly sensitive, multi-parameter (ratiometric) luminescent thermometer that operated in the cryogenic to high temperature range. The highest relative sensitivity (nearly 2% K^{-1}) was achieved for the 448/500 nm luminescence intensity ratio, which was associated with the Stark components of 4f–4f emission of Tm^{3+} and d–f emission of Tm^{2+}.

1. Introduction

Luminescence, which is the phenomena of conversion of energy into light upon excitation with different types of luminescent sources, has led to the development of diverse phosphor materials. Advancements in developing high-quality luminescent materials have gained much attention for utilization in various fields owing to their unique characteristics, such as improved luminescence efficiency, enhanced thermal stability, and cost-effective operation.[1] Phosphor materials are potentially involved in developing several lighting devices, such as fluorescent lamps, phosphor-converted white light emitting diodes (pc-wLEDs), displays, optical thermometry, and self-reference optical thermometers.[2–9] Rare earth (RE)-doped phosphors are commonly employed in solid-state lighting technologies to fabricate high-energy, efficient, durable, environment-friendly, sustainable and human-centric sustainable lighting sources. Another extensively investigated area for RE-doped phosphor applications is luminescence thermometry, which is a technique that enables remote detection of temperature by monitoring thermal evolution of the selected spectroscopic parameters.

The mostly used approach to produce white light is by amalgamating blue LED with yellow phosphor. However, this approach faces some drawbacks such as low color rendering index (CRI) and high correlated color temperature (CCT). Moreover, the blue component present in the white light generated *via* this approach affects the human body clock and poses an increased risk for diseases, such as damages to the endocrine system, sleep disorders and eye diseases.[10–12] In order to avoid the above-mentioned issues, the near UV (nUV)-driven wLEDs (*i.e.* n-UV

[a] Optical Materials Group, School of Sciences (Physics), National Institute of Technology Andhra Pradesh, Tadepalligudem, West Godavari District, Andhra Pradesh, 534101, India. E-mail: arunkumar@nitw.ac.in, arunkumar@nitandhra.ac.in
[b] Department of Physics, National Institute of Technology, Warangal, Hanamakonda, Telangana, 506004, India
[c] Department of Materials Science, School of Technology, Central University of Tamil Nadu, Thiruvarur, Tamil Nadu, 610 005, India
[d] Department of Rare Earths, Faculty of Chemistry, Adam Mickiewicz University, ul. Uniwersytetu Poznańskiego 8, 61-614, Poznań, Poland

† Electronic supplementary information (ESI) available. See DOI: https://doi.org/10.1039/d4tc05342g

‡ These authors contributed equally to this work.

LED chips with red-, green- and blue-emitting phosphor-based wLEDs) can act as an efficient alternative.

LEDs are expected to be fabricated using luminescent materials with better thermal stabilities. Temperature-dependent photoluminescence analysis are performed to confirm the fitness of phosphor materials in several applications. Thermal stability is a property related to the chemical composition and crystal structure rigidity of inorganic phosphors in the temperature range of interest.[13,14] An increase in the operating temperature affects the PL intensity of several phosphor materials. This phenomenon can be termed as 'thermal quenching', which occurs due to an increase in the number of non-radiative relaxations. Therefore, researchers are interested in developing phosphor materials that aid in mitigating the emission losses with the enhancements in operation temperatures. The anti-thermal quenching mechanism results in the delay of positive thermal quenching, zero thermal quenching, or abnormal quenching.[15,16] If the emission peak has a combination of any two thermal quenching mechanisms, it can be utilized for several applications. There is a high demand to prepare blue-emitting phosphor materials that meet the criterion of high thermal stability, a longer life-span and excellent luminous efficiency to achieve sustainable luminescent materials.

It is crucial to choose efficient host and activator combinations to develop luminescence material. RE ions can serve as potential candidate activators, due to their 4f–4f and 4f–5d transition. Owing to the numerous applications in visible and infrared regions, the evolution of thulium-based phosphor material holds significant importance. For developing blue-emitting phosphor materials, it is necessary to explore new dopant ions. In this context, Tm^{3+} ion can be chosen as a suitable activator ion due to its spectroscopic advantages, simplest energy level and efficient blue emission in the visible region. Thulium ion possess several emissions corresponding to transitions such as $^1D_2 \rightarrow {}^3F_4$, $^1D_2 \rightarrow {}^3P_0$, $^1I_6 \rightarrow {}^3H_4$ and $^1G_4 \rightarrow {}^3H_6$.[17]

The host plays an important role in realizing an efficient phosphor material through the establishment of a wide band-gap, high optical transparency, and excellent lumen output. Among the host materials available for the RE doped phosphor material, calcium dialuminate holds significant interest due to its excellent properties. Calcium dialuminate crystallizes in monoclinic structure having a $C2/c$ space group. Calcium dialuminate ($CaAl_4O_7$) has two crystallographic sites: Ca and Al. The calcium site is surrounded by five oxygen atoms. Aluminum has two inequivalent sites connected with four oxygen atoms and forms an AlO_4 tetrahedral structure. The Tm^{3+} ions seem to occupy one six-coordinated Ca site of the three available sites in monoclinic $CaAl_4O_7$. In the monoclinic $CaAl_4O_7$ structure, there are two six coordinated sites available with an average Ca–O distance of 2.40 Å and one nine coordinated site available with an average Ca–O distance of 2.58 Å. The six-coordinate site Ca–O average distance is shorter for Tm^{2+} compared with the nine-coordinated site Ca–O average distance. This prefers the substitution of Tm^{2+} in the nine-coordinated Ca^{2+} site. For coordination number six and nine, the sum of the ionic radii of Tm^{2+} and O^{2-} are 2.43 and 2.49 Å, respectively. This declares the probable occupation of Tm^{2+} in a nine-coordinated Ca site. In case of Tm^{3+}, the sum of the ionic radii of Tm^{3+} and O^{2-} are 2.28 and 2.45 Å for six and nine coordinated sites, respectively. This supports the substitution of Tm^{3+} in the six-coordinated Ca^{2+} site in $CaAl_4O_7$.

Phosphor-in-glass (P-i-G) structures have become a feasible and efficient alternative for lighting applications and have evolved as an effective technology. Owing to the difficulties faced in P-i-S, the P-i-G structure has some limelight.[18] The phosphors that are integrated in P-i-G structures will function as a down converter that will absorb the energy of lower wavelength and emit in higher wavelength and the glass matrix offers thermal and mechanical stabilities to the phosphor material, enabling it to preserve the luminescence properties of the phosphor material and it possesses high transparency.[19,20]

As temperature is the most important physical parameter, its constant and online control is critical, leading to the growing interest in luminescence thermometry, *i.e.* non-invasive and rapid detection of temperature.[21,22] Inorganic materials doped with various lanthanide (Ln) ions are the most commonly applied in optical temperature sensing owing to their unique electronic structure, thermalization of states and multicolor emission.[23] The following Ln ions are typically used for luminescence thermometry: Nd^{3+}, Pr^{3+}, Er^{3+} and Tm^{3+}. This is because they have thermally coupled levels (excited states) separated with a smaller energy difference with ΔE = 200–2000 cm^{-1} and hence, this property of temperature-dependent luminescence intensity ratio (LIR) is convenient for temperature detection.[21] However, the inherent drawback in this approach is their limited relative sensitivity to ΔE, as well as issues with calibration within extreme temperature ranges (beyond Boltzmann's law).[24,25]

Here, we address these issues and develop a novel strategy for temperature detection based on simultaneous emission of the rarely observed Tm^{2+} ions combined with PL of Tm^{3+}. Since there is no literature data pertaining to the synthesis of Tm^{3+}-doped $CaAl_4O_7$ phosphor, this motivated us to prepare an efficient blue emitting phosphor material through the microwave-assisted combustion route, and the fabrication of a P-i-G structure based on phosphor. The structural, vibrational, morphology and spectroscopic characteristics analysis were explored and reported in a systematic manner to understand the efficiency of the material for the lighting application. Temperature-dependent PL analysis (−180 to 300 °C) was performed to explore the thermal stability and temperature sensing performance of the material. We developed a novel ratiometric luminescent thermometer operating from a cryogenic to high temperature range with high sensitivity, reaching almost 2% K^{-1} thanks to diverse thermal quenching rates and thermalization processes of Tm^{2+} and Tm^{3+} emissions. This was possible by applying the 448/500 nm luminescence intensity ratio associated with the Stark component of Tm^{3+} 4f–4f emission and d–f emission of Tm^{2+}. Moreover, the unusual enhancement in the signal intensity with temperature may be very beneficial in the potential utilization of the obtained phosphors in LED devices, as well as in general lighting technology.

2. Experimental strategy

2.1. Synthesis of phosphor and fabrication of P-i-G material

2.1.1. Precursors required for the preparation of phosphor materials. Precursors such as calcium nitrate ($Ca(NO_3)_2$), aluminum nitrate ($Al(NO_3)_3$), thulium oxide (Tm_2O_3), urea and nitric acid were taken as starting materials. Nitric acid was used for the conversion of thulium oxide to thulium nitrate. All the chemicals were of high purity. In the process, the metal nitrates act as oxidizing agents. Fuel such as urea acts as a reducing agent that facilitates the combustion reaction. The precursors were taken in stoichiometric proportion to help the yield of the desirable phosphor materials homogenously. The following reaction was used to prepare nano-phosphor materials:

$$(1-x)Ca(NO_3)_2 + 4Al(NO_3)_3 + (O/F)\ NH_2CONH_2 + xTm(NO_3)_3 \rightarrow Ca_{(1-x)}Al_4O_7{:}xTm^{3+} + CO_2 \uparrow + H_2O \uparrow + N_2$$

where (O/F) represents the oxidizer-to-fuel ratio, 'x' is the dopant concentration, where x = 0.0075, 0.01, 0.03, 0.05, 0.07, and 0.09 mol.

2.1.2. Synthesis procedure. The microwave-assisted combustion synthesis route was used to synthesize single-phased thulium doped calcium dialuminate ($Ca_{(1-x)}Al_4O_7{:}xTm^{3+}$, $0.0075 \leq x \leq 0.09$) phosphor material. In general, the main aspect influencing the dimensionality of the resultant sample is the synthesis route and the various steps involved in it. The straightforward, cost-effective, and simple synthesis strategy involved in the microwave-assisted synthesis route renders it convenient for the preparation of phosphor materials. First, all the precursors in the metal nitrate form were dissolved with distilled water in a beaker. The solution was stirred with the help of a glass stirrer to obtain a homogeneous solution. Then, urea was added to the solution and stirred continuously. Subsequently, the solution was heated for a shorter span of time with the help of a hot plate to yield a gel-like solution. The beaker loaded with the gel-like substance was placed inside the microwave oven operating at 900 W programmed for 5 min. Combustion of the material occurred within a short period of time and the product was foamy. The foamy material was harvested, ground, and annealed with the help of a high temperature furnace operating at temperature at 1000 °C for 2 h. The resultant phosphor material was yielded in a powder form and scrutinized using structural and spectroscopic characterizations.

2.1.3. Fabrication of P-i-G structure. P-i-G material was fabricated by taking a specially designed borate-based glass system and the optimized $CaAl_4O_7{:}Tm^{3+}$ phosphor. First, the borate-based glass system was prepared through the melt-quenching method. Then, the glass was ground to a fine powder using a ball mill set-up. A desired amount of the glass and phosphor powder were taken and thoroughly mixed in a ball-mill set up. Subsequently, the phosphor and glass mixture were transferred to a recrystallized alumina crucible of high purity and was kept inside a furnace maintained at a high temperature for a fixed duration. The molten mixture was poured on a brass plate which was heated in another furnace operating at 400 °C. Then, the furnace was cooled down to room temperature and the resultant P-i-G solid was obtained. This substance was polished and cut into desired shape for further characterization and analysis (Fig. 3d).

2.2. Characterization

Powder X-ray diffraction (XRD) patterns of all the samples were recorded using a Bruker D8 advance X-ray spectrometer by maintaining the step-size of 0.020°, involving CuK_α (λ = 1.5406 Å) radiation between 10–70° for structural analysis. The XRD pattern of fabricated P-i-G was recorded using a Bruker D8 advance X-ray spectrometer between 10–80°. The refinement of the data concerning the lattice parameter of the Tm^{3+} doped $CaAl_4O_7$ sample was acquired from the Rietveld analysis. A Fourier transform infrared (FTIR) spectrum of the sample was recorded using a Bruker ALPHA II FTIR spectrophotometer. JASCO V-770 ultraviolet–visible (UV-VIS) spectrometer was used to record the absorption spectra of the prepared samples. Scanning electron microscopy (SEM) study was performed with the help of a FEI Quanta 250 field emission gun (FEG) scanning electron microscope with an energy dispersive analysis by X-ray (EDAX) detector. X-ray photoelectron spectroscopy (XPS) analysis was done using the UHV SPECS system equipped with an Mg anode as an electron source. The spectrum's position was calibrated for the binding energy of the C 1s orbital for the C–C chemical state (284.8 eV). In order to explore the luminescence properties, the excitation and emission spectra of the phosphor material were captured using a spectro-fluorimeter (model F-7000 FL spectrophotometer) equipped with a 150 W xenon lamp as the excitation source. PL decay curve of the prepared sample was recorded using a QuantaMaster 40 spectrophotometer equipped with a tunable energy laser Oppolette 355LD UVDM as the excitation source and Hamamatsu 928 photomultiplier as the detector (with repetition 20 Hz). Temperature-dependent PL measurements were performed using a Linkam THMS 600 temperature-controlled system. The fabricated P-i-G was polished using an Indfurr glass polisher.

3. Results and discussion

3.1. Structural analysis

The phase formation and crystallinity of the pure calcium dialuminate and Tm^{3+} doped calcium dialuminate samples were examined by analyzing the powder XRD patterns (Fig. 1(a)). The XRD peaks of each sample were well-matched with the standard JCPDS card no. – 023-1037 and crystallize in the monoclinic system possessing the space group of $C2/c$.[26,27] A small peak at 30° is observed that can be ascertained to aluminate. The volumetric fraction was less than 2%. With the variation of Tm^{3+} dopant concentration between 0.0075 to 0.09 mol, the diffraction peaks in the XRD pattern are in well-agreement with the JCPDS data that demonstrates the formation of the expected crystalline phase. There was no impact on the crystal structure of the material upon the introduction of

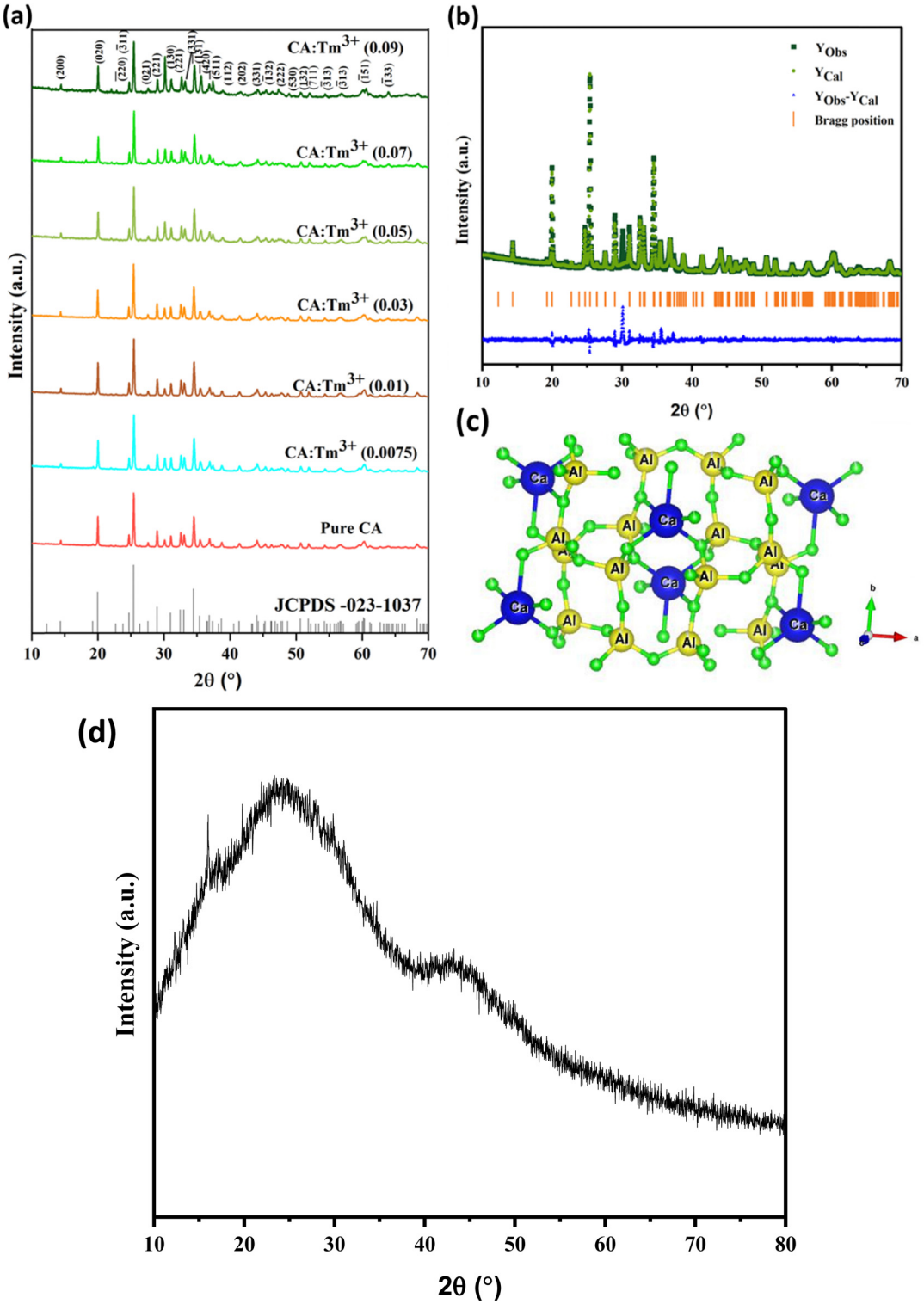

Fig. 1 (a) Powder XRD patterns of pure $CaAl_4O_7$ and Tm^{3+}-doped $CaAl_4O_7$ phosphor along with data of the JCPDS card 023-1037 (b) Refinement pattern of Tm^{3+} (3 mol%)-doped $CaAl_4O_7$ phosphor (c) Crystal structure of calcium dialuminate along with the Ca ion bonded with five oxygen and tetrahedral AlO_4. (d) XRD pattern of $CaAl_4O_7$:Tm^{3+} (0.03)-based phosphor-in-glass (P-i-G) structure.

the dopant (Tm^{3+}) ion. A slight shift towards higher angles (decrease in the interplanar spacing) of the recorded diffraction peaks is perceived for Tm^{3+} doped $CaAl_4O_7$ samples as the concentration increases from 0.0075 mol to 0.09 mol compared with pure calcium dialuminate. This is because of the smaller ionic radii (0.88 Å) of Tm^{3+} ions replacing the larger Ca^{2+} ions (1.00 Å), leading to a small decrease in the unit cell volume. The coordination number for the mentioned cations is VI.

To find the accurate site for the substitution of Tm^{3+} ion in the host matrix, it is essential to deduce the radius percentage difference (D_r%) between the cations involved. In accordance with the ionic radii of Ca^{2+} (1.00 Å), Al^{3+} (0.53 Å), and Tm^{3+} (0.88 Å) ions, the substitution of a Tm^{3+} ion in calcium ion site is anticipated. In case of site occupancy, the effective ionic radii of Ca^{2+} is 1.18 Å (CN = 9) and the ionic radii of Tm^{2+} are 1.09 Å (CN = 9) and 1.03 Å (CN = 6). Due to the similar ionic radii, the substitution of Tm^{2+} in the Ca^{2+} site is expected. However, computation of D_r% is crucial to determine the exact substitution of Tm^{3+} ion in the host. D_r% was determined using the following formula[28]:

$$D_r(\%) = \frac{[R_s(CN) - R_d(CN)]}{R_s(CN)} \times 100 \quad (1)$$

where in R_s indicates the ionic radii of the cation sites present in the host and R_d shows the ionic radii of the dopant. The value of D_r% should not be more than 30% for the preferential substitution.[29] The observed D_r% values for the Ca^{2+}/Tm^{3+} pair and Al^{3+}/Tm^{3+} pairs are 12% and −66.03%, respectively. These findings indicated that the Tm^{3+} ions are predicted to replace the six coordinated Ca^{2+} site in the $CaAl_4O_7$ host. The D_r% value for the Ca^{2+}/Tm^{2+} pair is 7.62%. This demonstrates the possible substitution of Tm^{2+} in the nine-coordinated Ca^{2+} site of $CaAl_4O_7$.

For the resultant phosphor material, the Rietveld profile fitting was performed by adopting the Fullprof software using the crystallographic data of pure calcium dialuminate and XRD data of $Ca_{(1-x)}Al_4O_7$:xTm^{3+}, x = 0.03 phosphor and (Fig. 1(b)). During the refinement procedure, the pseudo-Voigt function was chosen for the profile shape refinement. Throughout the refinement process, parameters such as scale factor, atomic positions, background, instrumental parameters, peak shape parameters, atomic occupancy and the lattice parameters were fitted. In Fig. 1(b), the black solid line signifies the calculated data and the red dotted line indicates the observed data experimentally. The refined parameters are shown in the Table 1. The obtained refined parameters and results are well matched with the standard data. It is observed that the sample crystallizes in monoclinic structure. From the refinement data, the following conclusions are drawn: (i) a decrease in unit cell volume is perceived for the Tm^{3+} doped calcium dialuminate sample compared to the pure $CaAl_4O_7$ suggests the successful incorporation of Tm^{3+} ion in the Ca^{2+} site; (ii) the slight mismatch in the ionic radii of Ca^{2+} (1.00 Å) and Tm^{3+} (0.88 Å) ions also favor the replacement of Ca^{2+} by Tm^{3+} ions.

Table 1 Refinement parameters of pure and $Ca_{(1-x)}Al_4O_7$:xTm^{3+}, x = 0.03 sample

Lattice parameters	Pure $CaAl_4O_7$[20]	$CaAl_4O_7$:Tm^{3+}
a (Å)	12.89	12.88
b (Å)	8.89	8.88
c (Å)	5.44	5.43
$\alpha = \gamma$ (°)	90	90
β (°)	106.93	107.01
Unit cell volume (Å^3)	596.47	595.87
Crystal structure	Monoclinic	Monoclinic
Space group	$C2/c$	$C2/c$

To acquire a deeper knowledge about the nature of environment within the crystal, the crystal structure of $CaAl_4O_7$ was drawn using the refinement data through the Vesta software (Fig. 1(c)). In $CaAl_4O_7$, there is one Ca^{2+} site that exists which is denoted as Ca1 (Fig. 1(c)). There are two inequivalent aluminum sites such as Al1 and Al2 as mentioned in the diagram. The Al^{3+} ions are connected with four oxygen ions, thereby manifesting the AlO_4 tetrahedral arrangement.

To estimate the crystallite size (D) of the sample, Scherrer's eqn (2) was employed by considering the main diffraction peak ($\bar{3}11$).[30]

$$D = \frac{k\lambda}{\beta \cos\theta} \quad (2)$$

where λ, β, and θ designate the X-ray wavelength, full-width-at-half-maximum and the Bragg's angle, and k is Scherrer's constant of 0.94. The estimated crystallite size of pure and Tm^{3+}-doped calcium dialuminate samples are presented in Table S1 in the ESI.† The computed crystallite size is between 38–44 nm.

Due to the very similar ionic radii, the Tm^{3+} ions have the probability to substitute in the calcium site, which aid in the creation of interstitial oxygen defects and calcium vacancies as a result of charge imbalance. In accordance with the Kröger–Vink notation, the probable situations for charge compensation are described as follows:[31]

$$2Tm^{3+} + 3Ca^{2+} \rightarrow [V_{Ca}]'' + 2[Tm_{Ca}]^{*} \quad (3)$$

$$2Ca^{2+} + 2Tm^{3+} \rightarrow 2[Tm_{Ca}]^{*} + O_i'' \quad (4)$$

where $[V_{Ca}]$ signifies the calcium vacancy comprising two negative charges and O_i indicates the oxygen defect with two negative charges.

The XRD pattern of the $CaAl_4O_7$:Tm^{3+} (0.03) based P-i-G structure was recorded in the 2θ range of 10–80° (Fig. 1(d)). The broad nature in the lower angle of the XRD pattern demonstrates the dominating amorphous nature in the fabricated P-i-G. The absence of the characteristic diffraction peak of $CaAl_4O_7$:Tm^{3+} (0.03) phosphor material is mainly due to the incorporation of a minimal amount of the phosphor material in the P-i-G structure.

3.2. Surface morphology and elemental composition

To analyze the morphology of the prepared samples, an SEM study of $CaAl_4O_7$:Tm^{3+} (3 mol%) was recorded (Fig. 2(a)). The SEM picture reveals that the morphology of the sample possesses a small portion of pores and voids which can be generated from the gases liberated during the combustion process (Fig. 2(a)). The morphology of the sample is a plate-like structure. The average particle size was estimated as ≈11 μm using ImageJ software and the normal particle size distribution plot.

The elemental composition of the prepared sample can be understood by recording the EDAX spectra. The EDAX spectra of $CaAl_4O_7$:Tm^{3+} (3 mol%) detected peaks associated with Ca, Al, O and Tm (Fig. 2(b)). The weight percentage of Ca, Al, O and Tm were 18.05, 37.25, 43.16 and 1.54%, respectively (Table inset

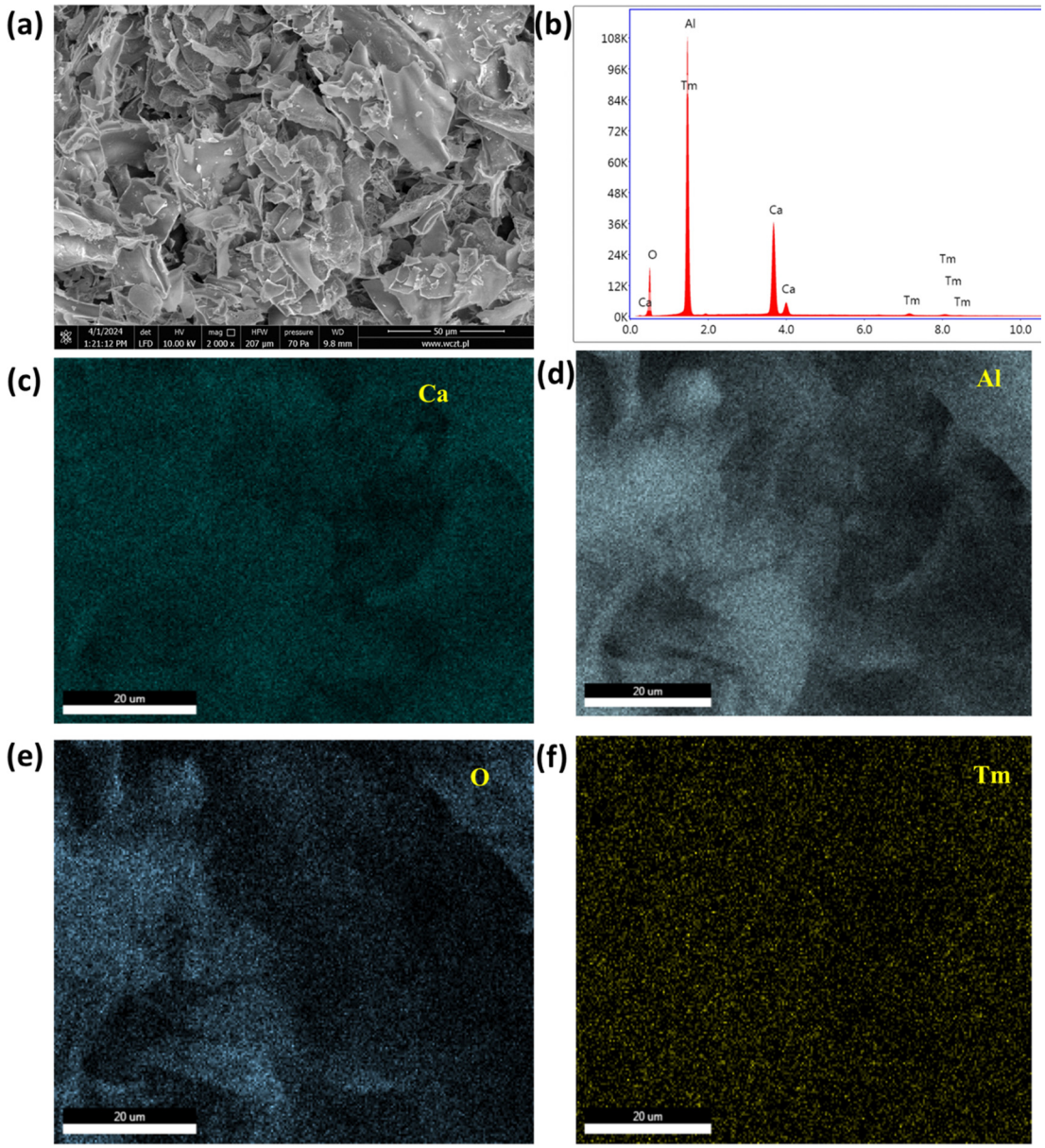

Fig. 2 (a) SEM image, (b) EDAX spectra (c–f) elemental analysis of $CaAl_4O_7:Tm^{3+}$ (3 mol%).

of Fig. 2(b)). The expected weight% of each element matched well with the obtained weight% through EDAX analysis. This affirms the presence of the elements in the stoichiometric amount in the yielded phosphor material. The elemental mappings of these elements are depicted in Fig. 2(c–f). This reveals the presence and homogeneous distribution of Ca, Al, O and Tm elements in the prepared phosphor.

3.3. FT–IR spectral analysis

An FT–IR study was conducted to examine the vibrational bands that can be found in the material and determine the phonon energies using the versatile KBr pellet technique. The FT–IR spectra of the $Ca_{(1-x)}Al_4O_7:xTm^{3+}$ (x = 0.05) sample was collected between 4000–400 cm^{-1} wavenumbers (Fig. 3(a)). The spectra illustrate the vibrational bands that are located around 3443 and 1454 cm^{-1} which are appear as a result of stretching and bending vibrations of –OH and CO_3^{2-} groups that are triggered by the moisture present in the sample evolved during the sample preparation time. The constant region in the range 3300–1500 cm^{-1} does not contain any peaks since no appropriate bond is present in the material that is characteristic of that region. The peaks situated at 532, 634 and 802 cm^{-1} are associated with Al–O bonding, and stretching and bending of the AlO_4 tetrahedral functional groups, respectively.[27] Hence, the maximum phonon energy for the material studied is around 800 cm^{-1}.

3.4. UV-vis absorption analysis

Fig. 3(b) elucidates the absorbance spectra of $Ca_{(1-x)}Al_4O_7:xTm^{3+}$ (x = 0.03) phosphor material between 200–800 nm to investigate

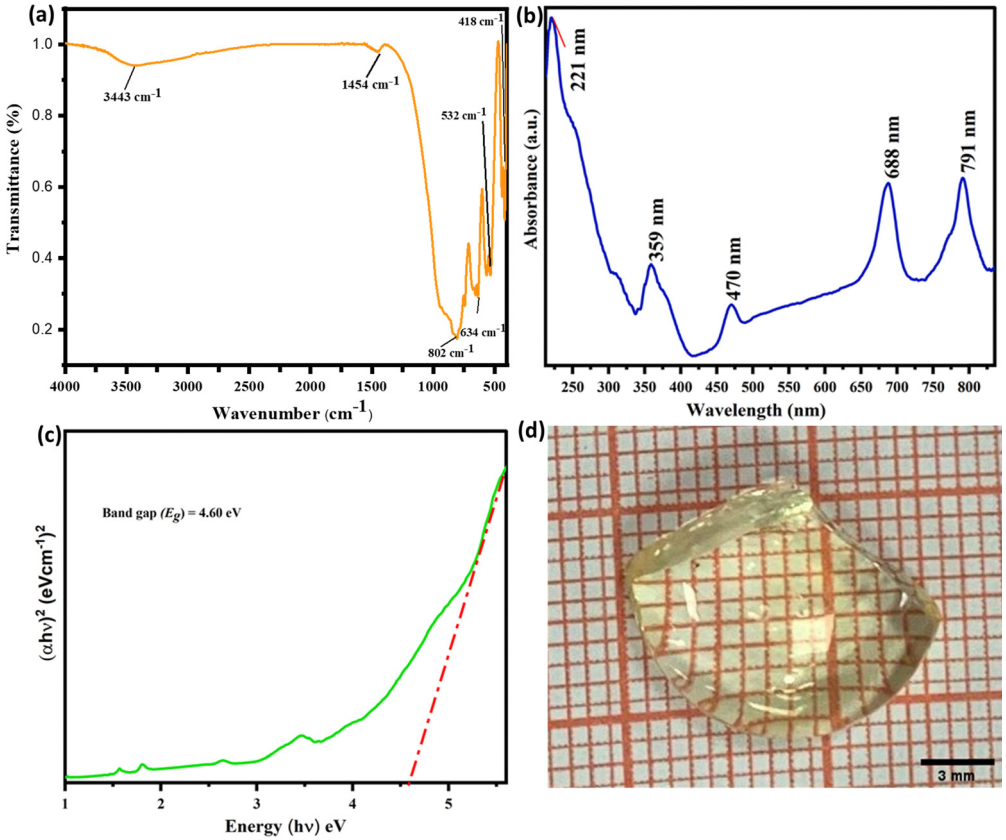

Fig. 3 (a) FTIR spectra of $CaAl_4O_7$:Tm^{3+} phosphor material. (b) Absorption spectra and (c) Tauc plot of $Ca_{(1-x)}Al_4O_7$:xTm^{3+} (x = 0.03) phosphor material (d) Fabricated phosphor-in-glass based on optimized $CaAl_4O_7$:Tm^{3+} phosphor.

the absorption characteristics and optical bandgap of the material. The resultant sample shows remarkable absorbance bands between 350–800 nm that can be assigned to the 4f–4f transitions of the Tm^{3+} ion. The absorption at 359, 470, 688 and 791 nm are assigned to the transition from the ground state $^3H_6$ to the excited energy state $^1D_2$, $^1G_4$, $^3F_3$, and $^3H_4$, respectively of the Tm^{3+} ion.[32] The intense absorption peak at 221 nm has mainly arisen due to the host absorption band. The bandgap of the sample can be computed by employing Tauc relation between the absorption coefficient and the bandgap in accordance with eqn (5).[33]

$$(\alpha h\nu)^{1/n} = A\,(h\nu - E_g) \quad (5)$$

where in α, $h\nu$, E_g, and A are the absorption coefficient, photon energy, bandgap and a constant, respectively. The parameter 'n' has values of 1/2 (allowed indirect), 2 (allowed direct), 3/2 (forbidden indirect) and 3 (forbidden direct) demonstrating the nature of the bandgap. Fig. 3(c) illustrates Tauc plot of Tm^{3+} ion doped calcium dialuminate phosphor material. The bandgap of the sample is computed to be 4.60 eV.

3.5. PL spectral analysis of $CaAl_4O_7$:Tm^{3+} phosphor

3.5.1. Excitation spectra of $CaAl_4O_7$:Tm^{3+} phosphor. For assessing the viability of the resultant phosphor material in various lighting applications, the PL measurement is a key criterion to be understood. The PL excitation spectra of the $Ca_{(1-x)}Al_4O_7$:xTm^{3+} (x = 0.03) phosphor were collected between 200–400 nm with the emission wavelength set at 459 nm (Fig. 4(a)). The excitation peaks are centered around 262, 275, 286 and 359 nm, because of the 4f–4f intra-configurational transitions that are assigned to the electronic transitions of the Tm^{3+} ions from their ground state ($^3H_6$) to various excited states such as $^3P_2$, $^3P_1$, $^1I_6$ and $^1D_2$, respectively.[34,35] The most prominent excitation peak around 359 nm shows that it can be employed to record the emission spectra of the sample. As a result, the specified phosphor is effectively excited by the near ultra-violet (NUV) light source. All the excitation peaks that are detected in the NUV region are in better agreement with the features observed in the absorbance spectra of the material.

3.5.2. Emission spectra of $CaAl_4O_7$:Tm^{3+} phosphor. The energy level diagram of Tm^{3+} ions can be employed to understand the emission spectra characteristics of the resulting phosphor materials. Upon 359 nm excitation, the electrons available in the ground state ($^3H_6$) are prompted to the higher energy levels ($^3P_2$, $^3P_1$, $^1I_6$, and $^1D_2$) by absorbing the excitation energy from the light source. After reaching the higher excited energy levels, the excited electrons relax to the lower excited state non-radiatively and then revert to the ground state ($^1D_2$–$^3F_4$) and emit visible light (Fig. 4(b)). The shaded rectangular area denotes the position of the excited $4f^{12}5d^1$ configuration of Tm^{2+}, which will be discussed in the next section.

The emission characteristics of all the doped samples *i.e.*, $Ca_{(1-x)}Al_4O_7$:xTm^{3+} ($0.0075 \leq x \leq 0.09$) phosphors are

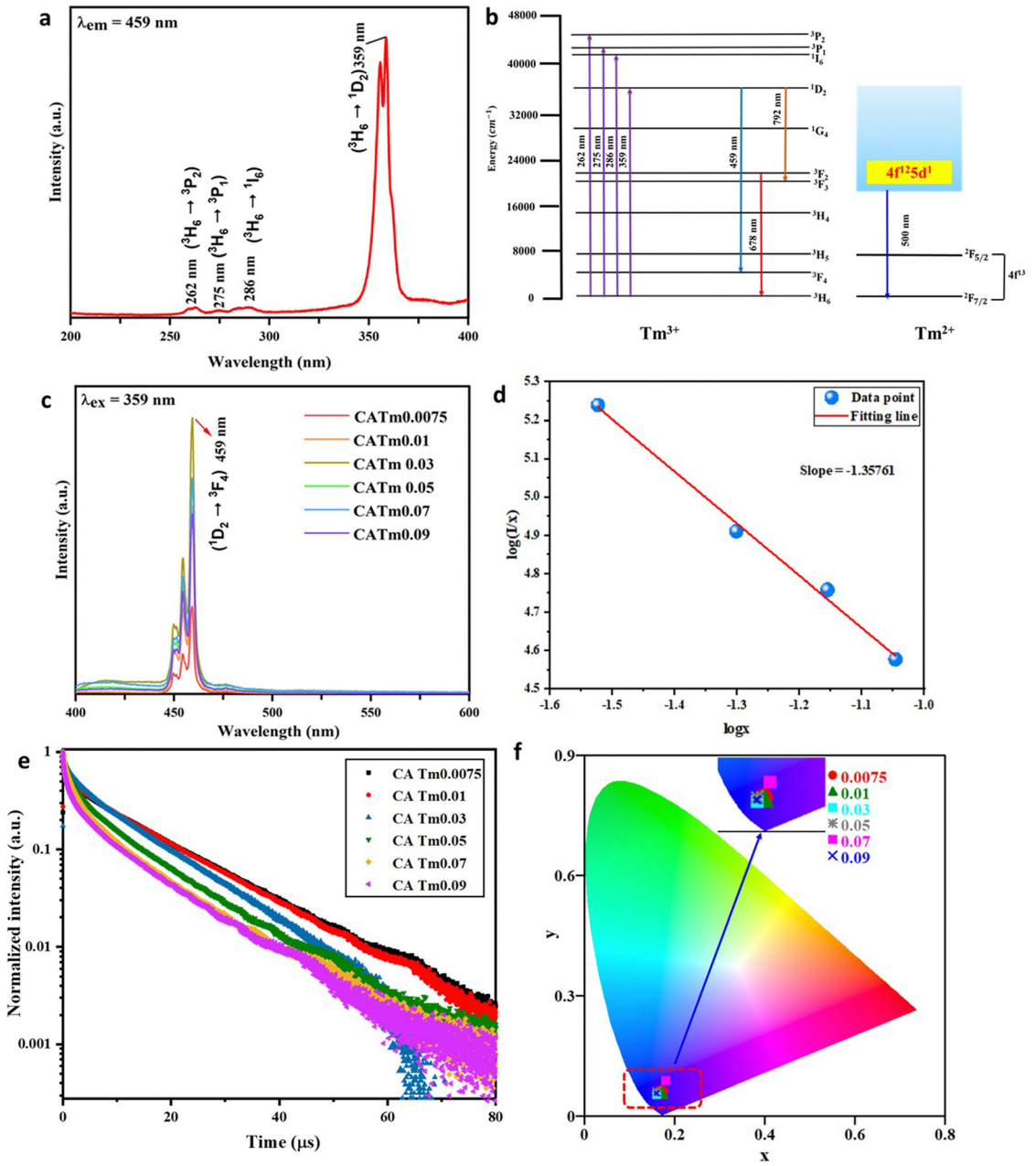

Fig. 4 (a) PL excitation spectra of $Ca_{(1-x)}Al_4O_7$:xTm^{3+} (x = 0.03) sample. (b) Energy-level diagram of Tm^{3+} ions. (c) PL emission spectra of $Ca_{(1-x)}Al_4O_7$:xTm^{3+} (0.0075 ≤ x ≤ 0.09) phosphor. (d) Plot of log$x$ *vs.* log (I/x); (e) PL decay curves of $CaAl_4O_7$:Tm^{3+} samples with varying Tm^{3+} concentration; (f) CIE chromaticity diagram of $CaAl_4O_7$:Tm^{3+} (Tm^{3+} concentration = 0.0075, 0.01, 0.03, 0.05, 0.07, and 0.09) sample.

understood by analyzing the PL emission spectra. The emission spectra of the resultant phosphors are documented with the excitation wavelength maintained at the optimal level of 359 nm in ambient temperature (Fig. 4(c)). The resulting emission spectra of all the phosphors have emission peak around 459 nm associated with the $^1D_2$–$^3F_4$ transition (Tm^{3+} ions) and the peak at 678 nm can be attributed to $^3F_2$–$^3H_6$ transitions (Tm^{3+} ions).[36,37] Splitting in the emission peaks is perceived because of the Stark effect and the strong crystal field effect.

The emission spectra for all dopant concentrations of the designated phosphor ($Ca_{(1-x)}Al_4O_7$:xTm^{3+}, 0.0075 ≤ x ≤ 0.09) were displayed in Fig. 4(c) to demonstrate the effect of concentration on the intensity of the signature peaks of Tm^{3+} ions. From Fig. 4(c), it is evident that upon increment in Tm^{3+} ion concentration, there is an enhancement in the PL emission intensity up to 3 mol%. However, on further increase in Tm^{3+} ion concentration, the intensity of the characteristic peak follows a diminishing trend owing to the mechanism of concentration quenching. The concentration quenching mechanism is mainly because of the non-radiative energy transfer that rely on the critical distance (R_c) *i.e.*, the distance between neighboring activator ions. With an increment in Tm^{3+}

ion concentration, the separation among the nearest ions tend to decrease, which leads to a stronger interaction between the neighbouring ions, thereby strengthening the non-radiative energy transfer process. There are three phenomena that are accountable for the non-radiative energy transfer[38]: (i) radiation reabsorption; (ii) exchange interaction; and (iii) multipolar interaction. Radiation reabsorption comes into picture if there is spectral overlap between the excitation and emission spectra. However, by considering the critical distance (R_c) calculation, the possibility of the other two mechanisms *i.e.* exchange interaction and multipolar interaction can be assessed. The exchange interaction mechanism occurs if the critical distance between the activator ions becomes less than 5 Å and multipolar interaction occurs when the R_c value exceeds 5 Å. To understand the mechanism accountable for the non-radiative energy transfer process among the neighboring activator ions, the R_c was deduced using following formula[39]:

$$R_c = 2\left[\frac{3V}{4\pi x_c N}\right]^{\frac{1}{3}} \quad (6)$$

where V is the unit cell volume of the resultant sample, x_c is the critical concentration of the sample, and N is the number of cation sites that are available per unit cell. By adopting eqn (6), the critical distance was 21.1 Å. Since the critical distance is higher than 5 Å, the multipolar interaction is the cause for concentration quenching.

The multipolar interaction is of three types: dipole–dipole, dipole–quadrupole and quadrupole–quadrupole interactions. Dexter's theory helps to infer the nature of interaction that exist between the neighboring activator ions using the following equation:[40–42]

$$\frac{1}{x} = K\left[1 + \beta(x)^{\frac{S}{3}}\right]^{-1} \quad (7)$$

where I denotes the emission intensity, while K and β are considered as constant. S value of 6, 8 and 10 inform the nature of the multipolar interaction. The S value was evaluated as 4.07 from the slope of the plot of log (I/x) *vs.* log (x) (Fig. 4(d)). Since this value is closer to 6, it suggests that the non-radiative energy transfer in the resultant sample is due to the dipole–dipole interactions.

However, the concentration quenching mechanism can be further explained based on the charge compensation model. The Tm^{3+} ions are dispersed throughout the $CaAl_4O_7$ host matrix when the Tm^{3+} ion concentration is low. The distance between the activator ions decreases with increasing dopant concentration. When the dopant concentration increases to a level that exceeds the critical concentration, the energy transfer phenomena may not follow eqn (6).[43] Charge neutrality mechanism can have two possibilities as discussed in Section 3.1.

The expected substitution of Tm^{3+} ion in the calcium site is determined from D_r% computation. Upon the substitution, two types of defects will be generated that act as the electron capture center. The calcium vacancy with two negative charges ($[V_{Ca}]''$) will create the dipole complex comprising defects as ($2[Tm_{Ca}]^*$–$[V_{Ca}]''$) upon the substitution of Tm^{3+} in Ca^{2+} site. Along with this, the second type of defect will be generated by the interstitial anion *i.e.* some of the oxygen atoms will reside in the interstitial site due to the creation of a dipole complex of ($2[Tm_{Ca}]^*-O''_i$). These lattice defects act like an electron trapping center. During PL, the activated electrons move from the ground state to higher excited states when the phosphor material is excited with the excitation source, and some part of electron will get trapped in the electron trapping center. The energy transfer process will occur between the Tm^{3+} ions and the trapping centers. During the transition of the excited electrons back to the ground state, these trapped electrons will not participate in the luminescence process, which reduces the luminescence intensity in the emission spectra of the sample.

3.5.3. PL decay time analysis. The PL decay time plot for all the samples were recorded for the emission attributed to the transition $^1D_2$–$^3F_4$ (Tm^{3+} ion) with the emission wavelength at 459 nm and the excitation wavelength set at 359 nm. The decay profiles could be fitted with the single exponential function mentioned in eqn (8).[44]

$$I = A + I_0 \exp(-t/\tau) \quad (8)$$

where in parameter I denotes the emission intensity at time t, A is the fitting parameter (amplitude), τ denotes the decay time, and I_0 denotes the emission intensity at time t = 0. The decay curves were plotted for the samples with varying Tm^{3+} ion concentrations (Fig. 4(e)). The decay time for all the samples are between 7.11–3.61 μs. With the increase in Tm^{3+} ion concentration (0.0075, 0.01, 0.03, 0.05, 0.07, and 0.09), the decay times shorten to 7.10, 7.11, 6.46, 5.11, 4.23 and 3.61 μs, respectively. The lifetime gradually shortens with increasing dopant concentration due to the concentration quenching mainly governed by the cross-relaxation processes.

3.6. Colorimetric properties

Commision Internationale de I'éclairage (CIE) chromaticity co-ordinates are significant elements to deduce the performance of the phosphor material in lighting applications. Each point in the CIE diagram can be termed as CIE chromaticity coordinates (x, y), where x refers to the color of the emission and y represents the saturation of the color. CIE chromaticity co-ordinates give an insight about the particular color of emission from the source. Chromaticity co-ordinates of the resultant phosphor material can be determined from the CIE diagram which can be plotted by adopting the PL emission data of the sample. The CIE diagram of the Tm^{3+} ion doped calcium dialuminate sample (Tm^{3+} ion concentration = 0.0075, 0.01, 0.03, 0.05, 0.07, and 0.09) showed that the emission color of the phosphor material was in the blue region (Fig. 4(f)). The presence of the CIE co-ordinates in the blue region illustrates the ability of the sample as a blue emitting phosphor. The CIE co-ordinates for the synthesized material is tabulated in Table S2 in the ESI.† The chromaticity co-ordinates for the optimized phosphor ($CaAl_4O_7$:Tm^{3+} (0.03)) was found to be x = 0.158, 0.054.

Correlated color temperature (CCT) of a material can be defined as the color emitted from the test lighting source that resemble a particular temperature on the black-body curve that

generates a specific color similar to the test lighting source. CCT authenticates the warmness or coolness nature of the light emitted from the source. The term 'correlated' comes into picture because the emission color of the light source is measured in kelvin to relate it with the temperature of a black-body. The color temperature of a lighting source also carries information on the appearance of the emitted color to a normal human eye. By utilizing McCamy's approximation as mentioned in eqn (9), the correlated color temperature of the sample can be estimated.[37,45]

$$\mathrm{CCT} = -449n^3 + 3525n^2 - 6823n + 5520.33 \quad n = \frac{(x - x_e)}{(y - y_e)} \tag{9}$$

where (x, y) is the co-ordinate of the sample that is obtainable from the CIE diagram and (x_e, y_e) signifies the chromaticity epicenter having the value of (0.186, 0.332). CCT values of the prepared samples were computed with the variation in Tm^{3+} ion concentration (Table S2 in the ESI†). It is inferred that the CCT value lies within 1620–1780 K for all the samples, which denotes the emission in the warmer region. For the optimized sample (0.03 mol of Tm^{3+} ion), the CCT value was determined to be 1623 K, which is desirable for practical applications.

To understand the applicability of a sample in lighting technology, it is necessary to analyze the color purity of the emitted color from the sample. Color purity is the extent to which a color emitted from the light source resembles its hue. A hue represents a pure color without mixing of tints and shades. The hue of the color can be used to generate different colors of tints and shades by adding an appropriate amount of white and black color to it, respectively.

Color saturation or color purity can be determined by taking the ratio of the distance between the CIE co-ordinate point of the emitted light and the equal energy source and the distance between the dominant wavelength point and the illuminant energy point. By utilizing the formula mentioned in eqn (10), the color purity of the sample can be established.[46]

$$\text{Color purity}\,(\%) = \frac{\sqrt{(x - x_{ee})^2 + (y - y_{ee})^2}}{\sqrt{(x_d - x_{ee})^2 + (y_d - y_{ee})^2}} \times 100 \tag{10}$$

where in (x, y), (x_{ee}, y_{ee}) and (x_d, y_d) indicates the chromaticity co-ordinates, equal energy point co-ordinates and dominant wavelength point, respectively. The determined color purity for the optimized phosphor ($CaAl_4O_7$:Tm^{3+} (3 mol%)) of 91.96% demonstrated the superior color purity of the sample.

3.7. Temperature-dependent PL study

Temperature-dependent PL measurements were performed for the optimized phosphor $CaAl_4O_7$:Tm^{3+} (0.03) in the temperature range from −180 to 300 °C, and it is depicted in Fig. 5(a). From Fig. 5(a), it is clear that the position of the emission bands in the spectra do not significantly change with temperature. However, both the intensity and shape of the bands vary with temperature, leading to the gradual change of the emission color from greenish-blue to deep-blue, as illustrated in the CIE diagram in Fig. 5(b). The most evident phenomenon is the appearance of the broad emission band between approximately 400 to 600 nm in the cryogenic T-range. This band is associated with allowed inter-configurational d–f emission of Tm^{2+} ($4f^{12}5d^1 \rightarrow 4f^{13}$), which can coexist together with Tm^{3+} in the $CaAl_4O_7$ material. This host and an $SrAl_2O_4$ analogue are both good stabilizers of divalent lanthanides ions.[47–51] However, the available literature data mainly report on Eu^{2+}, whereas this is the first report on stabilization of the rarely observed Tm^{2+} in the $CaAl_4O_7$ material. Another spectroscopic evidence of the presence of Tm^{2+} is a thermally induced enhancement of Tm^{3+} emission bands, correlated with a significant decrease in intensity of the broad-band emission of Tm^{2+} (Fig. 5(c)). The observed phenomena are associated with thermalization processes between the excited 4f ($^1D_2$ state) and $4f^{12}5d^1$ configurations of Tm^{3+} and Tm^{2+}, respectively, as well as differences in thermal quenching rates for the mentioned emission. The approximated energy of the excited $4f^{12}5d^1$ configuration of Tm^{2+} (deduced from the emission spectra) in respect to the energies of the Tm^{3+} excited states is given in the energy level diagram discussed earlier (Fig. 4(b)). It is clear that there is an equilibrium between the $^1D_2$ state of Tm^{3+} and the excited $4f^{12}5d^1$ configuration of Tm^{2+}, which are energetically close together. However, the excited configuration of Tm^{2+} has lower energy than the $^1D_2$ state of Tm^{3+}, resulting in a broad-band emission of Tm^{2+} only in the cryogenic T-range. This is because there is plausibly some thermal excitation of the electrons from the excited $4f^{12}5d^1$ configuration of Tm^{2+} to the $^1D_2$ state of Tm^{3+} with temperature elevation, *i.e.* a temperature-induced interionic crossover,[52] leading to diminished broad band emission and enhanced narrow-band emission of Tm^{3+}. On the other hand, the differences in thermal quenching rates of the inter and intra-configurations transitions may contribute to the observed effects as well. Additionally, Fig. 5d shows the integrated intensities of the selected Stark components of the $^1D_2 \rightarrow {}^3F_4$ transition as a function of temperature, revealing the expected thermalization between the high-energy (centered at ≈448 nm) and low-energy (≈456 nm) crystal-filled components.

Due to the above-mentioned thermal effects, the intensity of the blue emission band (450 nm) at 150 °C is approximately 115% of its intensity at room temperature. Such unusual enhancement in the signal intensity may be very beneficial in the potential utilization of the obtained phosphors in lighting technology. For practical applicability, the operating temperature of the lighting source is 150 °C and the material is considered to be a good candidate for a phosphor for lighting technology when its intensity is at the indicated temperature of around 75% (or higher) of the initial intensity at ambient conditions. The superior performance of the developed material makes it a promising candidate as a blue phosphor in general lighting and LED technology.

To confirm the presence of Tm^{2+} in the synthesized material, we investigated the XPS spectrum for $CaAl_4O_7$:$Tm^{2+/3+}$ from 0 to 1200 eV binding energy (Fig. S1a, ESI†) to confirm the

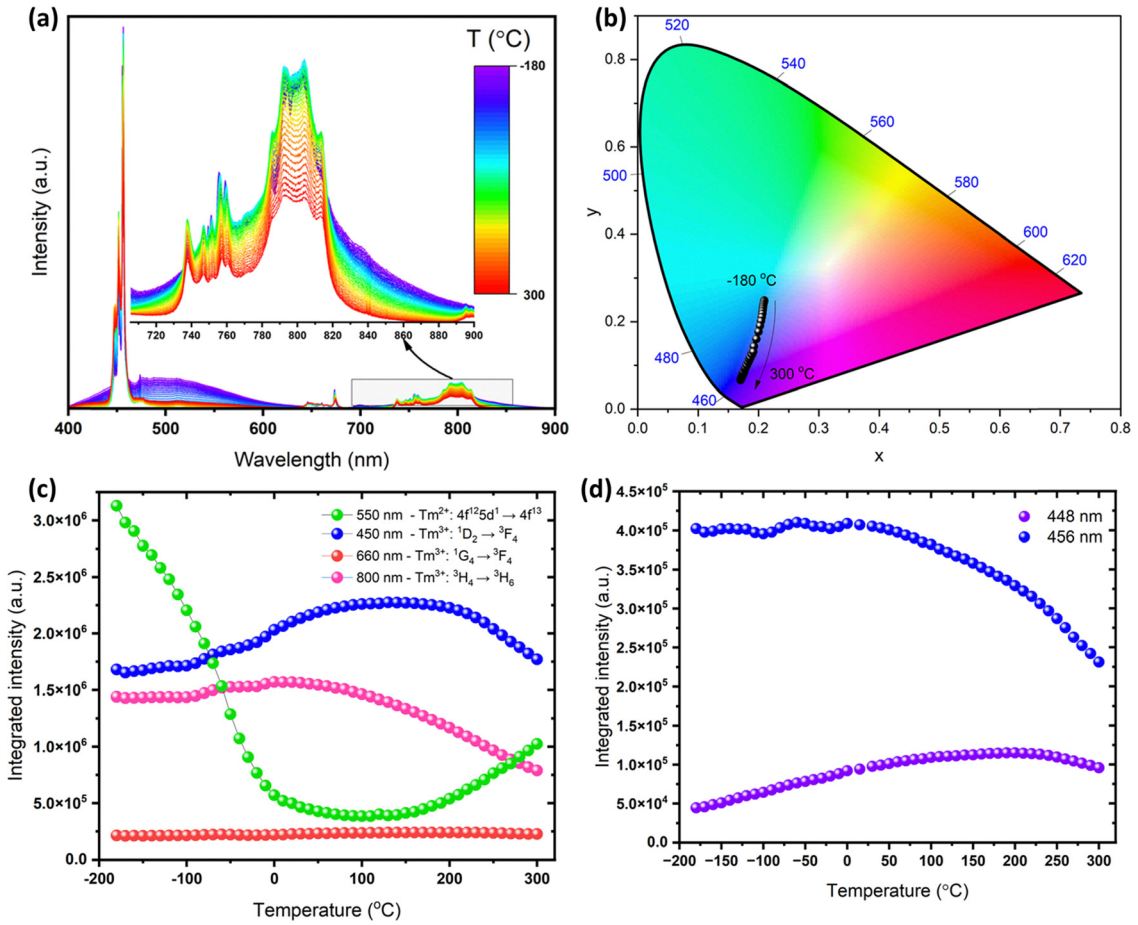

Fig. 5 (a) Temperature-dependent PL spectra of $CaAl_4O_7$:$Tm^{2+/3+}$ (0.03) recorded in the T-range of −180 to 300 °C. (b) CIE color diagram based on the temperature-dependent emission spectra. (c) Integrated emission intensities of Tm^{2+} and Tm^{3+} as a function of temperature. (d) Integrated emission intensities of the selected Tm^{3+} Stark components ($^1D_2 \rightarrow {}^3F_4$ transition) as a function of temperature.

presence of the Tm^{3+} and Tm^{2+} in the synthesized material. In the full spectrum range, we observed intense bands from O 1s, Ca 2p, C 1s, and Al 2p orbitals (Fig. S1a, ESI†). Unfortunately, the signal in the region of the Tm was not very intense due to the very low content of Tm ion in the material (3%), and it can be only observed in the magnified spectrum (Fig. S1b, ESI†). In the magnified spectrum, we can clearly distinguish bands for the Tm 4d orbital between 170–185 eV, which agrees with the literature values for Tm^{3+} ions.[53] Only a small fraction of the Tm^{3+} ions were reduced to a divalent Tm^{2+} state in the material, resulting in a very low content of Tm^{2+}. Therefore, the signal intensity of the Tm^{2+} band was extremely low in the XPS spectrum. Nonetheless, the visible bands between 165–170 eV, *i.e.*, the main band with a maximum at 166.9 eV and satellite band at 168.8 eV, confirm the presence of the Tm^{2+} ion in the synthesized $CaAl_4O_7$:$Tm^{2+/3+}$ material.

We could determine several LIRs for various emission bands thanks to the abundance of electronic transition in the studied systems, as well as different temperature-dependent transition probabilities, thermal quenching rates and thermalization processes of the excited 4f ($^1D_2$ state) and $4f^{12}5d^1$ configurations of Tm^{3+} and Tm^{2+}, respectively. Fig. 6(a) shows thermal evolution of the LIR parameters based on Tm^{3+} and Tm^{2+} emissions: 660 nm (Tm^{3+})/500 nm (Tm^{2+}), 450 nm (Tm^{3+})/500 nm (Tm^{2+}) and 660 nm (Tm^{3+})/450 nm (Tm^{3+}). Initially, the 660/500 nm and 450/500 nm LIRs gradually increased with temperature and then started to decrease above ≈100 °C; meanwhile, the latter LIR monotonically decreased in the whole investigated T-range. Alternatively, we plotted LIRs based on two Stark components of Tm^{3+} emission band (456/448 nm), which also monotonically decreased with temperatures (Fig. 6b). The second LIR (448/500 nm) is based on a single Stark component of Tm^{3+} emission (448 nm) and Tm^{2+} emission (500 nm), which initially increased with temperature, and then began to decrease above ≈100 °C. Therefore, we only used the temperature ranges where the given LIR parameter changes in a monotonic way for fitting to ensure that the particular LIR value corresponds to a single temperature value. Due to the abundance of the possible temperature-governed radiative and non-radiative processes, complexity of the studied two ions system, contributions of alike thermal quenching and thermalization processes, and most importantly the lack of a well-established physical model describing the temperature evolution of such a multivalent (Tm^{2+}–Tm^{3+}) system, we used a

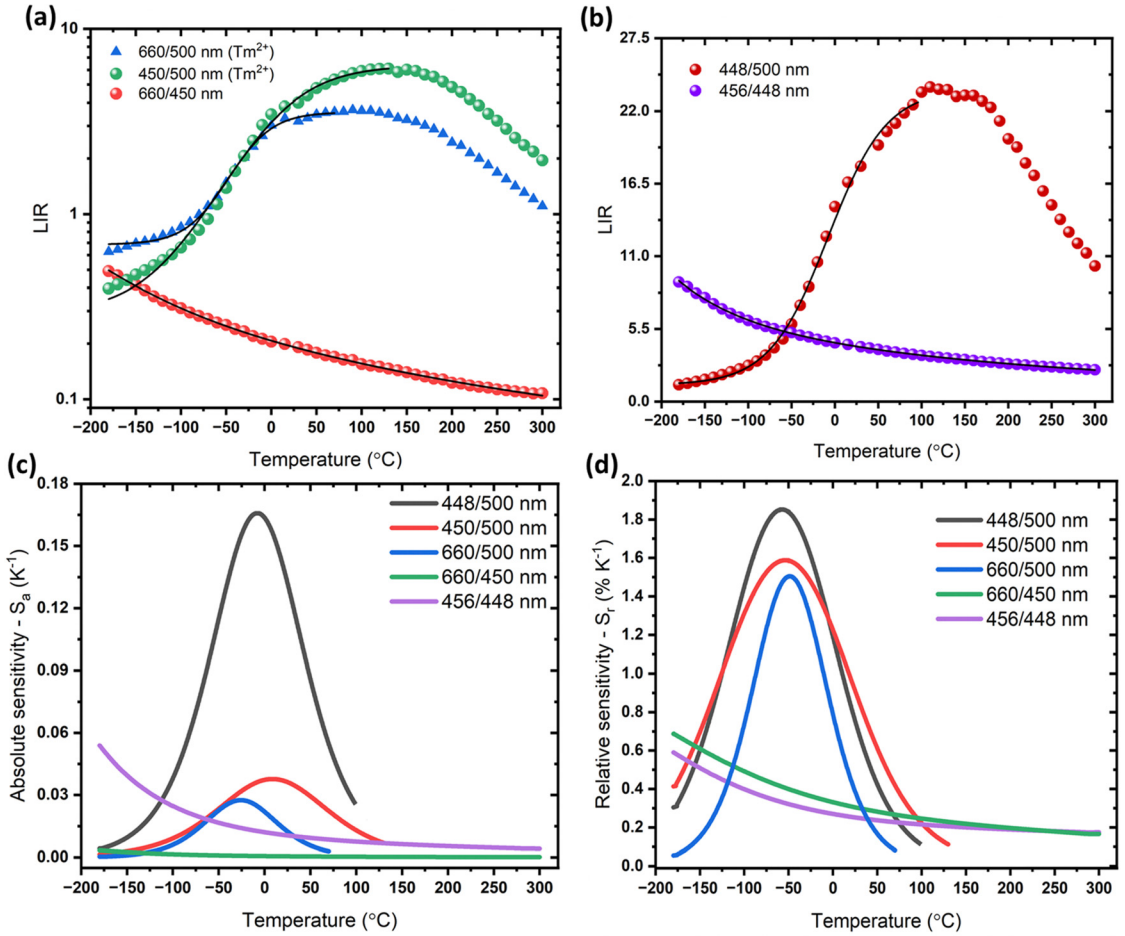

Fig. 6 (a) Determined LIR parameters, *i.e.* 660 nm/500 nm (Tm^{2+}), 450 nm/500 nm (Tm^{2+}) and 660 nm/450 nm; (b) (Stark) 448 nm/500 nm (Tm^{2+}) and (Stark) 456 nm/448 nm (Stark); and (c and d) the corresponding absolute (S_a) and relative thermal sensitivities (S_r) as a function of temperature for the $CaAl_4O_7$:$Tm^{2+/3+}$ material.

phenomenological (empirical) exponential functions to fit the determined data LIR parameters as a function of temperature:

$$\mathrm{LIR} = A\exp\left(\frac{T}{B}\right) \tag{11}$$

A similar protocol is typically applied in other literature reports on non-Boltzmann luminescent thermometers.[24,54–57] The fitting parameters used and the goodness of fits (R^2) are listed in Table S3 in the ESI.† Based on the thermal evolution of the obtained fitting lines (curves) we determined the absolute (S_a) and relative temperature sensitivity (S_r) for the given LIR thermometric parameter using the following formula:

$$S_a = \frac{\mathrm{dLIR}}{\mathrm{d}T} \tag{12}$$

$$S_r = 100\% \times \frac{1}{\mathrm{LIR}}\frac{\mathrm{dLIR}}{\mathrm{d}T} \tag{13}$$

In contrast to the S_a parameter, the S_r value allows quantitative comparisons of the sensing performance of different optical thermometers operating with different thermometer parameters, regardless of the optical setup used, and it is commonly expressed in % K^{-1}.[24,54] The S_r value shows how the measured spectroscopic parameter, LIR, changes per 1 K of the absolute temperature. Both S_a (0.165 K^{-1}) and S_r (1.85% K^{-1}) are the highest for the LIR 448/500 nm (Stark line of Tm^{3+}/Tm^{2+}), with maxima at around 0 and −50 °C, respectively. This is due to a significant decrease of Tm^{2+} intensity with temperature and enhancement of the high-energy Tm^{3+} crystal-field component caused by thermalization processes. The LIRs including the emission of Tm^{2+} allow detection at least from −180 °C up to around 130 °C, because at higher temperatures these LIR parameters take the same values as those at lower temperature (the derivative/sensitivity change sign from positive to negative or *vice versa*), which could lead to the erroneous readouts. Hence, it is recommended to use thermometric parameters exclusively based on Tm^{3+} emissions for thermal sensing at higher temperatures. The S_r values of various thulium-containing temperature sensing materials are compared with the present material under investigation (Table 2). It can be concluded that the $CaAl_4O_7$:$Tm^{2+/3+}$ material exhibits appreciable performance and it can operate between cryogenic and high temperatures. The Tm^{3+}/Tm^{2+} band intensity ratio shows better sensitivity than other reported sensors solely based on Tm^{2+} ions.

Table 2 Comparison of the relative sensitivity (S_r) of various temperature-sensing material

Material	Temperature range (K)	Maximum relative sensitivity (S_r) (% K^{-1})	T [K]	Ref.
$YAlO_3$:Tm^{3+}	324 to 425	0.26	324	58
$NaNbO_3$:Tm^{3+}	303 to 343	0.8	303	59
$BaMoO_4$:Tm^{3+}–Yb^{3+}	298 to 498	1.36	309	60
Y_2O_3:Tm^{3+}/Yb^{3+}	224 to 798	1.01	341.79	61
Y_2O_3:Tm^{3+}, Eu^{3+}	303 to 503	0.46	303	62
$LaPO_4$:Yb^{3+}–Tm^{3+}	293 to 773	0.50	293	63
SrB_4O_7:Tm^{2+}	13 to 180	1.48	82	64
$CaAl_4O_7$:$Tm^{2+/3+}$	93 to 573	1.85	223	This work

3.8. Blue emitting P-i-G structure

To assess the applicability and potential of the synthesized phosphor material in the lighting industry, we fabricated the P-i-G structure by taking the optimized $Ca_{(1-x)}Al_4O_7$:xTm^{3+} (x = 0.03) phosphor and a specially designed borate glass system (Fig. 3(d)). The fabricated P-i-G material was excited with nUV excitation and emission occurred. This clearly states the uniform presence of phosphor material in the glass matrix.

To validate the suitability of the fabricated P-i-G for the application, photometric quantities such as luminous efficacy of radiation (LER) and luminous efficiency were computed by recording the PL emission spectra of the fabricated P-i-G.

Luminous efficacy of radiation is a vital quantity which denotes the percentage of visible radiation from the total light emitted from the light source that can be perceived through a normal human eye.

Luminous efficacy (LE) of radiation can be found by utilizing eqn (14).[65,66]

$$\mathrm{LE} = \frac{\int I(\lambda)V(\lambda)\mathrm{d}\lambda}{\int I(\lambda)\mathrm{d}\lambda} \times 683\,\mathrm{lm\,W^{-1}} \quad (14)$$

where in Is(λ) denotes the emission spectra of the fabricated P-i-G and V(λ) signifies the spectra that corresponds to human eye sensitivity. Here, 683 lm W^{-1} represents highest luminous efficacy owing to the reason that a normal human eye has maximum eye sensitivity at 555 nm.

LE of the sample can be computed using eqn (15).

$$\mathrm{LE}\,(\%) = \frac{\text{Luminous efficacy}}{683\,\mathrm{lm\,W^{-1}}} \times 100 \quad (15)$$

By using eqn (15) and (16), the luminous efficacy and luminous efficiency of the fabricated P-i-G structure was determined to be 251.42 lm W^{-1} and 36.81%, respectively, which validated the suitability of the fabricated P-i-G for application in lighting devices.

4. Conclusions

Here, we show the first report on the simultaneous presence of divalent and trivalent thulium ions (Tm^{2+} and Tm^{3+}) in the $CaAl_4O_7$ material, *i.e.* structure which can stabilize lanthanide ions at +2 and +3 oxidation states, as well as their great potential in luminescence thermometry and lighting technology, due to temperature-induced signal enhancement and opposite thermal evolution of intra-configurational (4f–4f) and inter-configurational (5d–4f) transitions of thulium ions. In this study, we successfully synthesized $CaAl_4O_7$ phosphor doped with thulium ions, exhibiting blue luminescence using a microwave-assisted combustion method, which was further used for the development of a P-i-G structure. The monoclinic crystalline structure was confirmed through powder XRD, and a wide bandgap of 4.60 eV was identified. The presence of Tm^{2+} and Tm^{3+} in the synthesized material was confirmed through the XPS study. Temperature-dependent measurements indicated the presence of Tm^{2+} ions, with a notable broad-band emission centered around 500 nm at cryogenic temperatures. The enhancement of the Tm^{3+} signal intensity with increasing temperature suggests potential applications in general lighting technology and LED devices. Moreover, the different thermal quenching rates and thermalization processes of Tm^{2+} and Tm^{3+} emissions enabled the development of a highly sensitive, multi-parameter ratiometric luminescent thermometer, effective across a wide temperature range from cryogenic conditions to elevated temperatures. The highest thermal sensitivity of almost 2% K^{-1} was achieved for the luminescence intensity ratio of 448/500 nm, linked to the Stark components of Tm^{3+} 4f–4f emissions and the 5d–4f emissions of Tm^{2+}. These findings highlight the potential of $CaAl_4O_7$ material doped with divalent and trivalent lanthanide ions as a promising, optically active component in advanced photonic applications, optical sensing and lighting technology.

Data availability

The data supporting this article have been included as part of the ESI.†

Conflicts of interest

The authors declare that they have no known competing financial interests or personal relationships that could have appeared to influence the work reported in this paper.

Acknowledgements

The authors are grateful to the administration of National Institute of Technology, Andhra Pradesh for extending the SEED Grant (Ref. No. NITAP/SD-G/17/2020 dated-05/11/2020). Authors are thankful to Science and Engineering Research Board (SERB) Project (Ref. No. CRG/2020/002153 dated 25/12/2020) sponsored by the Govt. of India. This work was supported by the National Science Centre, Poland (Grant no. 2023/50/E/ST5/00021). Authors acknowledge the support from the Department of Chemical Engineering, National Institute of Technology Andhra Pradesh for providing the FTIR facility.

References

1 B. Shao, J. Huo and H. You, Prevailing strategies to tune emission color of lanthanide- activated phosphors for WLED applications, *Adv. Opt. Mater.*, 2019, **7**, 1900319, DOI: **10.1002/adom.201900319**.

2 G. B. Nair, H. C. Swart and S. J. Dhoble, *Prog. Mater. Sci.*, 2020, **109**, 100622, DOI: **10.1016/j.pmatsci.2019.100622**.

3 A. Santra, N. Chakraborty, K. Panigrahi, K. K. Chattopadhyay and U. K. Ghorai, $SrTiO_3$:Sm^{3+}, Na^{+}- codoped orange-emitting nanophosphor for pc-WLEDs, *J. Mater. Sci.: Mater. Electron.*, 2022, **33**, 1–15, DOI: **10.1007/s10854-021-06876-5**.

4 Y. Li, Y. Zhou, X. Li, H. Wu, L. Zhao and W. Wang, Energy transfer and the anti-thermal quenching behavior of $Sr_8MgCe(PO_4)_7$:Tb^{3+} for temperature sensing, *Spectrochim. Acta, Part A*, 2021, **252**, 119548, DOI: **10.1016/j.saa.2021.119548**.

5 S. Gai, P. Gao, K. Chen, C. Tang, Y. Zhao, J. Wei, Y. Zhang, M. S. Molokeev, M. Xia and Z. Zhou, Superior Quantum Efficiency Blue-Emitting Phosphors with High Thermal Stability toward Multipurpose LED Applications, *Adv. Opt. Mater.*, 2024, **12**, 2302870, DOI: **10.1002/adom.202302870**.

6 Q. Yao, P. Hu, P. Sun, M. Liu, R. Dong, K. Chao, Y. Liu, J. Jiang and H. Jiang, YAG:Ce^{3+} Transparent Ceramic Phosphors Brighten the Next-Generation Laser-Driven Lighting, *Adv. Mater.*, 2022, **32**, 1907888, DOI: **10.1002/adma.201907888**.

7 P. Dang, Y. Wei, D. Liu, G. Li and J. Lin, Recent Advances in Chromium-Doped Near-Infrared Luminescent Materials: Fundamentals, Optimization Strategies, and Applications, *Adv. Opt. Mater.*, 2023, **11**, 2201739, DOI: **10.1002/adom.202201739**.

8 K. Li, D. Zhu and C. Yue, Codoping Pr^{3+} and Er^{3+} into $NaLaTi_2O_6$ to realize dual-mode FIR temperature sensing properties, *Spectrochim. Acta, Part A*, 2025, **326**, 125224, DOI: **10.1016/j.saa.2024.125224**.

9 K. Li, Z. Zhang, D. Zhu and C. Yue, Excellent temperature sensitivities based on the FIR technique of up-conversion luminescence in a novel $NaLaTi_2O_6$:Yb^{3+},Tm^{3+} material, *Inorg. Chem. Front.*, 2024, **11**, 7464–7474, DOI: **10.1039/D4QI01669F**.

10 S. Lai, M. Zhao, Y. Zhao, M. S. Molokeev and Z. Xia, Eu2+ Doping Concentration-Induced Site-Selective Occupation and Photoluminescence Tuning in $KSrScSi_2O_7$:Eu^{2+} Phosphor, *ACS Mater. Au*, 2022, **2**, 374–380, DOI: **10.1021/acsmaterialsau.1c00081**.

11 Y. Fu, P. Xiong, X. Liu, X. Wang, S. Wu, Q. Liu, M. Peng and Y. Chen, A promising blue-emitting phosphor $CaYGaO_4$:Bi^{3+} for near-ultraviolet (NUV) pumped white LED application and the emission improvement by Li+ ions, *J. Mater. Chem. C*, 2021, **9**, 303–312, DOI: **10.1039/D0TC03941A**.

12 H. Dai, X. Wang, Z. Liu, J. Zhang, X. Xu and G. Zhu, A long-term stable zero-thermal-quenching blue-emitting phosphor for sustainable and human-centric lighting, *J. Mater. Chem. C*, 2024, **12**, 11907–11915, DOI: **10.1039/D4TC02056A**.

13 F. Jahanbazi and Y. Mao, Negative Thermal Expansion Materials as Anti-Thermal-Quenching Phosphor Matrixes: Status, Opportunities, and Challenges, *Inorg. Chem.*, 2024, **63**, 8989–9001, DOI: **10.1021/acs.inorgchem.4c00329**.

14 Y. H. Kim, P. Arunkumar, B. Y. Kim, S. Unithrattil, E. Kim, S.-H. Moon, J. Y. Hyun, K. H. Kim, D. Lee, J.-S. Lee and W. B. Im, A zero-thermal-quenching phosphor, *Nat. Mater.*, 2017, **16**, 543–550, DOI: **10.1038/nmat4843**.

15 J. Liao, M. Wang, F. Lin, Z. Han, B. Fu, D. Tu, X. Chen, B. Qiu and H.-R. Wen, Thermally boosted upconversion and downshifting luminescence in $Sc_2(MoO_4)_3$:Yb/Er with two-dimensional negative thermal expansion, *Nat. Commun.*, 2022, **13**, 2090, DOI: **10.1038/s41467-022-29784-6**.

16 X. Tian, L. Guo, J. Wen, L. Zhu, C. Ji, Z. Huang, H. Qiu, F. Luo, X. Liu, J. Li, C. Li, Y. Peng, J. Cao, Z. He and H. Zhong, Anti-thermal quenching behavior of Sm^{3+} doped SrMoO4 phosphor for new application in temperature sensing, *J. Alloys Compd.*, 2023, **959**, 170574, DOI: **10.1016/j.jallcom.2023.170574**.

17 L. Guerbous, M. Derbal and J. P. Chaminade, Photoluminescence and energy transfer of Tm^{3+} doped $LiIn(WO_4)_2$ blue phosphors, *J. Lumin.*, 2010, **130**, 2469–2475, DOI: **10.1016/j.jlumin.2010.08.014**.

18 W. J. Chung and Y. H. Nam, Review-A Review on Phosphor in Glass as a High Power LED Color Converter, *ECS J. Solid State Sci. Technol.*, 2020, **9**, 016010, DOI: **10.1149/2.0142001JSS**.

19 M. Behera, R. Panda, P. Dhivya, D. Joshi and R. A. Kumar, Study of efficient sustainable phosphor in glass (P – i – G) material for white LED applications fabricated by tape casting and screen-printing techniques, *Mater. Sci. Eng. B.*, 2023, **298**, 116811, DOI: **10.1016/j.mseb.2023.116811**.

20 J. Deng, W. Li, H. Zhang, Y. Liu, B. Lei, H. Zhang, L. Liu, X. Bai, H. Luo and H. Liu, Eu^{3+}-doped phosphor-in-glass: a route toward tunable multicolor materials for near-UV high-power warm-white LEDs, *Adv. Opt. Mater.*, 2017, **5**, 1600910, DOI: **10.1002/adom.201600910**.

21 C. D. S. Brites, R. Marin, M. Suta, A. N. Carneiro Neto, E. Ximendes, D. Jaque and L. D. Carlos, Spotlight on Luminescence Thermometry: Basics, Challenges, and Cutting-Edge Applications, *Adv. Mater.*, 2023, **35**, 2302749, DOI: **10.1002/adma.202302749**.

22 X. Qiu, T. Zheng, M. Runowski, P. Woźny, I. R. Martín, K. Soler-Carracedo, C. Espinosa Piñero, S. Lebedkin, O. Fuhr and S. Bräse, Constructing [2.2]Paracyclophane-Based Ultrasensitive Optical Fluorescent-Phosphorescent Thermometer with Cucurbit[8]uril Supramolecular Assembly, *Adv. Funct. Mater.*, 2024, **34**, 2313517, DOI: **10.1002/adfm.202313517**.

23 N. Jurga, M. Runowski and T. Grzyb, Lanthanide-based nanothermometers for bioapplications: excitation and temperature sensing in optical transparency windows, *J. Mater. Chem. C*, 2024, **12**, 12218–12248, DOI: **10.1039/D3TC04716D**.

24 M. Runowski, P. Woźny, N. Stopikowska, I. R. Martín, V. Lavín and S. Lis, Luminescent Nanothermometer Operating at Very High Temperature—Sensing up to 1000 K with Upconverting Nanoparticles (Yb^{3+}/Tm^{3+}), *ACS Appl. Mater. Interfaces*, 2020, **12**, 43933–43941, DOI: **10.1021/acsami.0c13011**.

25 M. Runowski, S. Goderski, D. Przybylska, T. Grzyb, S. Lis and I. R. Martín, Sr_2LuF_7:Yb^{3+}–Ho^{3+}–Er^{3+} Upconverting

Nanoparticles as Luminescent Thermometers in the First, Second, and Third Biological Windows, *ACS Appl. Nano Mater.*, 2020, **3**, 6406–6415, DOI: 10.1021/acsanm.0c00839.

26 P. J. Baldock, A. Parker and I. Sladdin, X-ray powder diffraction data for calcium monoaluminate and calcium dialuminate, *J. Appl. Cryst.*, 1970, **3**, 188–191, DOI: 10.1107/S0021889870005952.

27 R. Panda, M. Behera, R. A. Kumar, D. Joshi and R. K. Padhi, Luminescence studies of high color purity red-emitting $CaAl_4O_7:Eu^{3+}$ phosphor prepared by microwave-assisted synthesis technique, *J. Alloys Compd.*, 2023, **968**, 171879, DOI: 10.1016/j.jallcom.2023.171879.

28 K. Cheng, Y. Xu, X. Liu, J. Long, W. Huang and C. Deng, A novel far-red phosphors $Li_2ZnTi_3O_8$: Cr^{3+} for indoor plant cultivation: synthesis and luminescence properties, *Ceram. Int.*, 2023, **49**, 6343–6350, DOI: 10.1016/j.ceramint.2022.11.169.

29 K. Cheng, Y. Xu, X. Liu, J. Long, W. Huang and C. Deng, A novel far-red phosphors $Li_2ZnTi_3O_8:Cr^{3+}$ for indoor plant cultivation: synthesis and luminescence properties, *Ceram. Int.*, 2023, **49**, 6343–6350, DOI: 10.1016/j.ceramint.2022.11.169.

30 M. R. Chandana, B. R. R. Krushna, J. Malleshappa, K. Manjunatha, T.-E. Hsu, S. Y. Wu, S. C. Sharma, B. D. Prasad, B. Subramanian and H. Nagabhushana, Simple fabrication of novel Sm^{3+} doped $BaGd_2ZnO_5$ nanophosphors for flexible displays, improved data security applications, and solid-state lighting applications, *Mater. Today Sustainability*, 2023, **22**, 100397, DOI: 10.1016/j.mtsust.2023.100397.

31 T. T. Deng, E. H. Song, J. Su, Y. Y. Zhou, L. Y. Wang, S. Ye and Q. Y. Zhang, *J. Mater. Chem. C*, 2018, **6**, 4418–4426, DOI: 10.1039/C8TC00689J.

32 F. Bougradja, M. Diaf, R. Fartas, H. Boubekri and S. Khiari, Photoluminescence investigations of Tm^{3+} doped SrF_2 single crystals for visible and infrared laser applications, *Opt. Mater.*, 2020, **108**, 110143, DOI: 10.1016/j.optmat.2020.110143.

33 N. H. Deepthi, G. P. Darshan, R. B. Basavaraj, B. Daruka Prasad and H. Nagabhushana, Large-scale controlled bio-inspired fabrication of 3D $CeO_2:Eu^{3+}$ hierarchical structures for evaluation of highly sensitive visualization of latent fingerprints, *Sens. Actuators, B*, 2018, **255**, 3127–3147, DOI: 10.1016/j.snb.2017.09.138.

34 W. T. Carnall, P. R. Fields and K. Rajnak, Electronic energy levels in the trivalent lanthanide aquo ions, Pr^{3+}, Nd^{3+}, Pm^{3+}, Sm^{3+}, Dy^{3+}, Ho^{3+}, Er^{3+}, and Tm^{3+}, *J. Chem. Phys.*, 1968, **49**, 4424–4442, DOI: 10.1063/1.1669893.

35 X. Wu, L. Du, Q. Ren and O. Hai, Enhancing the blue luminescence behaviour of the Na^+ Co-doped novel $LiLaSiO_4:Tm^{3+}$ phosphor, *Polyhedron*, 2021, **202**, 115209, DOI: 10.1016/j.poly.2021.115209.

36 A. Cheddadi, R. Fartas, M. Diaf and H. Boubekri, Spectroscopic investigations of Tm^{3+} doped CdF_2 single crystals and infrared laser potentialities, *J. Lumin.*, 2024, **265**, 120237, DOI: 10.1016/j.jlumin.2023.120237.

37 G. P. Darshan, H. B. Premkumar, H. Nagabhushana, S. C. Sharma, S. C. Prashantha, H. P. Nagaswarup and B. Daruka Prasad, Blue light emitting ceramic nano-pigments of Tm^{3+} doped $YAlO_3$: Applications in latent finger print, anti-counterfeiting and porcelain stoneware, *Dyes Pigm.*, 2016, **131**, 268–281, DOI: 10.1016/j.dyepig.2016.02.015.

38 M. Venkataravanappa, R. B. Basavaraj, G. P. Darshan, B. Daruka Prasad, S. C. Sharma, P. Hema Prabha, S. Ramani and H. Nagabhushana, Multifunctional Dy (III) doped di-calcium silicate array for boosting display and forensic applications, *J. Rare Earths*, 2018, **36**, 690–702, DOI: 10.1016/j.jre.2017.11.013.

39 N. Kucuk, Ümit H. Kaynar, S. Akca, Y. Alajlani, L. Yin, Y. Wang, J. Garcia Guinea, K. Bulcar, T. Dogan, Y. Karabulut, M. Ayvacikli, A. Canimoglu, M. Topaksu and N. Can, Enhancing the blue luminescence behaviour of the Li co-doped novel phosphor ZnB_2O_4: Tm^{3+}, *J. Alloys Compd.*, 2020, **838**, 155587, DOI: 10.1016/j.jallcom.2020.155587.

40 Y. Hua, K. Zhou, X. Wang and X. Qiu, Investigations on photoluminescence properties of rare-earth ion single-doped $CaSrSb_2O_7$ phosphors, *Inorg. Chem. Commun.*, 2022, **137**, 109197, DOI: 10.1016/j.inoche.2022.109197.

41 X. Xu, Q. Shao, L. Yao, Y. Dong and J. Jiang, Highly efficient and thermally stable Cr^{3+}-activated silicate phosphors for broadband near-infrared LED applications, *Chem. Eng. J.*, 2020, **383**, 123108, DOI: 10.1016/j.cej.2019.123108.

42 L. G. Van Uitert, Characterization of energy transfer interactions between rare earth ions, *J. Electrochem. Soc.*, 1967, **114**, 1048–1054, DOI: 10.1149/1.2424184.

43 G. P. Darshan, A. Arjun, H. B. Premkumar, G. Tamilarasu, S. C. Sharma, H. Nagabhushana and S. O. Manjunatha, Double perovskite structured $Ca_2MgWO_6:Sm^{3+}$ nanophosphor: Tailored for future-generation WLEDs and dosimetry applications, *J. Alloys Compd.*, 2023, **960**, 170662, DOI: 10.1016/j.jallcom.2023.170662.

44 R. K. Padhi, P. Vinodhkumar, S. Panda and B. S. Panigrahi, Deciphering the site occupancy and photoluminescence character of Sm^{3+} in dense-packed $Ca_3MgSi_2O_8$ nanocrystals using time-resolved emission spectroscopy, *Solid State Sci.*, 2021, **118**, 106647, DOI: 10.1016/j.solidstatesciences.2021.106647.

45 C. S. McCamy, Correlated color temperature as an explicit function of chromaticity coordinates, *Color Res. Appl.*, 1992, **17**, 142–144, DOI: 10.1002/col.5080170211.

46 M. Mangalagowri, R. B. Basavaraj, G. P. Darshan, M. S. Raju, Y. V. Naik, D. Kavyashree, H. K. Inamdar, S. C. Sharma and H. Nagabhushana, Sonochemical synthesis of green emitting $Ca_2SiO_4:Er^{3+}$ nanopowders: Promising applications in optical thermometry and radiation dosimeter, *Opt. Mater.*, 2019, **92**, 125–135, DOI: 10.1016/j.optmat.2019.04.005.

47 A. N. Yerpude and S. J. Dhoble, Combustion synthesis of blue-emitting submicron $CaAl_4O_7:Eu^{2+}$, Dy^{3+} persistence phosphor, *Luminescence*, 2012, **27**, 450–454, DOI: 10.1002/bio.1373.

48 A. Drozdowski, D. Poelman, M. Runowski, H. Hemmerich, F. Rivera-López and T. Grzyb, Unleashing the glow: upconverting nanoparticles recharge persistent luminescent materials – applications in 3D-printing and optical coding, *J. Mater. Chem. C*, 2024, **12**, 13040–13049.

49 R. Estefanía Rojas-Hernandez, F. Rubio-Marcos, M. Ángel Rodriguez and J. Francisco Fernandez, Long lasting

phosphors: $SrAl_2O_4$:Eu, Dy as the most studied material, *Renewable Sustainable Energy Rev.*, 2018, **81**, 2759–2770.

50 A. M. Achari, V. Perumalsamy, G. Swati and A. Khare, $SrAl_2O_4:Eu^{2+},Dy^{3+}$ Long Afterglow Phosphor and Its Flexible Film for Optomechanical Sensing Application, *ACS Omega*, 2023, **8**, 45483–45494.

51 C. Yuesheng, Z. Ping and Z. Zhentai, Eu^{2+} and Dy^{3+} co-doped $Sr_3Al_2O_6$ red long-afterglow phosphors with new flower-like morphology, *Phys. B*, 2008, **403**, 4120–4122.

52 T. Zheng, M. Runowski, P. Rodríguez-Hernández, A. Muñoz, F. J. Manjón, M. Sójka, M. Suta, E. Zych, S. Lis and V. Lavín, Pressure-driven configurational crossover between $4f^7$ and $4f^65d^1$ States – Giant enhancement of narrow Eu^{2+} UV-Emission lines in SrB_4O_7 for luminescence manometry, *Acta Mater.*, 2022, **231**, 117886.

53 T. Miyazaki, Y. Tokumoto, R. Sumii, H. Yagi, N. Izumi, H. Shinohara and S. Hino, Photoelectron spectra of thulium atoms encapsulated C_{82} fullerene, $Tm_2@C_{82}$ (III) and $Tm_2C_2@C_{82}$ (III), *Chem. Phys.*, 2014, **431–432**, 47–50.

54 C. D. S. Brites, R. Marin, M. Suta, A. N. Carneiro Neto, E. Ximendes, D. Jaque and L. D. Carlos, *Adv. Mater.*, 2023, **35**, 2302749.

55 T. Zheng, M. Runowski, P. Woźny, B. Barszcz, S. Lis, M. Vega, J. Llanos, K. Soler-Carracedo and I. R. Martín, *J. Alloys Compd.*, 2022, **906**, 164329.

56 C. D. S. Brites, K. Fiaczyk, J. F. C. B. Ramalho, M. Sójka, L. D. Carlos and E. Zych, *Adv. Opt. Mater.*, 2018, **6**, 1701318.

57 T. Zheng, M. Sójka, P. Woźny, I. R. Martín, V. Lavín, E. Zych, S. Lis, P. Du, L. Luo and M. Runowski, *Adv. Opt. Mater.*, 2022, **10**, 2201055.

58 M. A. Hernandez-Rodriguez, A. D. Lozano-Gorrin, V. Lavin, U. R. Rodriguez-Mendoza and I. R. Martin, Yttrium orthoaluminate nanoperovskite doped with Tm^{3+} ions as upconversion optical temperature sensor in the near-infrared region, *Opt. Express*, 2017, **25**, 27845.

59 A. F. Pereira, J. F. Silva, A. S. Gouveia-Neto and C. Jacinto, 1.319 μm excited thulium doped nanoparticles for subtissue thermal sensing with deep penetration and high contrast imaging, *Sens. Actuators, B*, 2017, **238**, 525–531.

60 X. Liu, R. S. Lei, Y. Y. Li and S. Q. Xu, Tm^{3+}/Yb^{3+}: $BaMoO_4$ phosphor for high-performance thermometry operating in the first biological window, *Opt. Lett.*, 2019, **44**, 3633–3636.

61 H. Zhou, K. Zhu, J. Wang, J. Qiu, L. Yue, L.-G. Wang and L. Ye, Effects of Yb^{3+} concentration on up-conversion luminescence and temperature sensing characteristics of $Tm^{3+}/Yb^{3+}:Y_2O_3$ phosphor, DOI: **10.2139/ssrn.4013634**, Available SSRN: **https://ssrn.com/abstract=4013634**.

62 H. Liu, Q. Meng and C. Wang, Optical Temperature Sensing Based on Linear Change of Luminescence Intensity Ratio in $Y_2O_3:Tm^{3+},Eu^{3+}$ Phosphors, *J. Fluoresc.*, 2025, **35**, 155–164.

63 M. Runowski, A. Shyichuk, A. Tyminski, T. Grzyb, V. Lavín and S. Lis, Multifunctional Optical Sensors for Nanomanometry and Nanothermometry: High-Pressure and High-Temperature Upconversion Luminescence of Lanthanide-Doped Phosphates-$LaPO_4/YPO_4:Yb^{3+}–Tm^{3+}$, *ACS Appl. Mater. Interfaces*, 2018, **10**, 17269–17279.

64 T. Zheng, M. Sójka, M. Runowski, P. Woźny, S. Lis and E. Zych, Tm^{2+} Activated SrB_4O_7 Bifunctional Sensor of Temperature and Pressure - Highly Sensitive, Multi-Parameter Luminescence Thermometry and Manometry, *Adv. Opt. Mater.*, 2021, **9**, 2101507.

65 S. Kaur, A. K. Vishwakarma, N. Deopa, A. Prasad, M. Jayasimhadri and A. S. Rao, Spectroscopic studies of Dy^{3+} doped borate glasses for cool white light generation, *Mater. Res. Bull.*, 2018, **104**, 77–82, DOI: **10.1016/j.materresbull.2018.04.002**.

66 T. Kang, S. Lee, T. Kim and J. Kim, Efficient Luminescence of $Sr_2Si_5N_8:Eu^{2+}$ nanophosphor and its film applications to LED and Solar cell as a downconverter, *Sci. Rep.*, 2020, **10**, 1475, DOI: **10.1038/s41598-020-58469-7**.